



# Studying the preparation, characterization, and physical properties of NiFe<sub>2</sub>O<sub>4</sub>, TiO<sub>2</sub>, and NiFe<sub>2</sub>O<sub>4</sub>/TiO<sub>2</sub> nanocomposite

Dalia N. Ghaffar<sup>1</sup> · M. M. Arman<sup>1</sup> · S. I. El-Dek<sup>2</sup> · Rania Ramadan<sup>1</sup>

Received: 7 November 2023 / Accepted: 20 February 2024 / Published online: 29 March 2024  
© The Author(s) 2024

## Abstract

NiFe<sub>2</sub>O<sub>4</sub> nanoparticles have been synthesized using the flash auto-combustion technique, while TiO<sub>2</sub> nanoparticles were prepared via sol–gel method. NiFe<sub>2</sub>O<sub>4</sub>/TiO<sub>2</sub> nanocomposite was obtained through the sonochemical method. Investigated samples have been studied through XRD, FTIR, and FESEM. The crystallite sizes of NiFe<sub>2</sub>O<sub>4</sub>, TiO<sub>2</sub>, and NiFe<sub>2</sub>O<sub>4</sub>/TiO<sub>2</sub> are 48.37, 25.56, and 32.46 nm, respectively. FTIR analysis was used to look into the materials' functional groups. The images of FESEM illustrated that the particles were prepared in nanoscale. All samples were good absorbers in the UV spectrum through the wavelengths of 200–350 nm. The energy band gap values of TiO<sub>2</sub>, NiFe<sub>2</sub>O<sub>4</sub>, and NiFe<sub>2</sub>O<sub>4</sub>/TiO<sub>2</sub> nanocomposite are 3.4, 2.3, and 2.5 eV, respectively, for the indirect transition. The samples' dielectric characteristics have been investigated and they have a semiconductor like behavior. VSM and the Faraday technique were used to test the materials' magnetic characteristics.

**Keywords** Nanocomposite · TiO<sub>2</sub> · NiFe<sub>2</sub>O<sub>4</sub> · Magnetization

## 1 Introduction

MeFe<sub>2</sub>O<sub>4</sub> nanostructures (Me = Fe, Ni) are considered to be one of the most important nano ferrites due to their potential for various applications. One of the key aspects of spinel ferrite class is nickel ferrite [1], which has generated a lot of research interest. Nickel ferrite [2] adopted inverse spinel structure and possesses a saturation magnetization (M<sub>s</sub>) of 23.604 eV/g and a coercivity (H<sub>c</sub>) of 207.92Oe [1]. Experimentally, the direct transition optical band gap (E<sub>g</sub>) is reported to be 4 eV, while for indirect transition, it was 2 eV [2].

Due to its exceptional properties, it is used in a wide-spread range of applications, such as: electrocatalytic, non-volatile memory, nanofibrillate, nano-biomass, low dielectric losses power applications [3–7]. As a result, different

types of nano-structures based on Ni ferrite have been developed in the last few years using several techniques [8–11].

TiO<sub>2</sub> is a non-toxic oxide, chemically stable against photo-corrosion with high oxidizing power [9]. However, TiO<sub>2</sub> has some limitations for use in photocatalytic applications. It has a wide band gap E<sub>g</sub> (3.0 eV for rutile, 3.2 eV for anatase), responding only to ultraviolet (UV) irradiation that corresponds to the wavelength of 390 nm for photoactivation. Some modifications for the solar irradiation response of TiO<sub>2</sub> should be enhanced to reduce its E<sub>g</sub>. Lately, the formation of a composite of TiO<sub>2</sub> with magnetic MFe<sub>2</sub>O<sub>4</sub> is a gorgeous field of study because MeFe<sub>2</sub>O<sub>4</sub> (Me: Fe, Ni) nanoparticles have too narrow E<sub>g</sub> to be a good sensitizer for wide E<sub>g</sub> semiconductors (CoFe<sub>2</sub>O<sub>4</sub>: 1.10 eV, ZnFe<sub>2</sub>O<sub>4</sub>: 1.9 eV, NiFe<sub>2</sub>O<sub>4</sub>: 1.56 eV) [12–14]. They revealed astonishing trends such as suitable tunable band positions, numerous redox states, low cost, thermal stability in addition to the easiness of preparation [15–19].

Depending on the external magnetic field intensity, composites made of ferromagnetic materials display faster rates of pollutant degradation [20]. It has also been renowned that easy electron migration through the interface arises when the alignment of magnetic moments produced by the composite is the same for all constituent parts [21]. Additionally, it has been anticipated that charge-carrier recombination can be

✉ M. M. Arman  
mmarmsci@gmail.com; mmarmsci@cu.edu.eg

<sup>1</sup> Materials Science Lab (1), Physics Department, Faculty of Science, Cairo University, Giza, Egypt

<sup>2</sup> Materials Science and Nanotechnology Department, Faculty of Postgraduate Studies for Advanced Sciences, Beni-Suef University, Beni-Suef, Egypt

repressed by modifying the electron spin polarization states of the photocatalysts through doping, morphology changes and modifying the structure. Using spin-orbital or hyperfine coupling, such magnetic semiconductors allow for the flipping of the electron's spin state [22]. Most crucially, the photocatalytic composite that is formed of magnetic material is easy to recover once the photocatalytic process is terminated. A magnetic photocatalyst is effortlessly acquired where it can be reused for water treatment procedures [23, 24] since the gained material can easily be contaminated.  $\text{MeFe}_2\text{O}_4/\text{TiO}_2$  is essential and commonly employed in photocatalytic applications due to its ability to degrade organic hazardous chemicals [11, 13, 20–22].

Resistive switching (RS)-based memristor devices have been used in many different applications because of their superior switching performance [25–28]. Given that  $\text{TiO}_2$  is a potential model material to explore several nameless resistive phenomena [29, 30], the simple RS device structure makes them appropriate for use in the development of advanced computers and future technologies (metal–insulator–metal) and high efficiency with low power consumption [31, 32]. Positive exceptional electrical features that are not reachable with conventional oxide–oxide or ferrite–ferrite nanocomposites can be attained by merging two distinct material classes into a nanocomposite [33]. The RS phenomenon is presently present in many materials, such as transition metal oxides [34, 35] and perovskite oxides [36, 37].

In this piece of work,  $\text{NiFe}_2\text{O}_4$ ,  $\text{TiO}_2$  nanoparticles and their nanocomposite were prepared using simple, fast and low cost technique. We also aimed to better understand their physical, optical, and electronic structures to estimate their proper applications.

## 2 Experimental techniques

### 2.1 Constituents

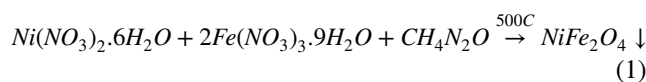
Nickel nitrate, iron nitrate, Ti isopropoxide, ethanol, and urea with chemical formula  $(\text{Ni}(\text{NO}_3)_2 \cdot 0.6\text{H}_2\text{O}, 99\%)$ ,  $(\text{Fe}(\text{NO}_3)_3 \cdot 9\text{H}_2\text{O}, 99\%)$ ,  $(\text{Ti}\{\text{OCH}(\text{CH}_3)_2\}_4)$ ,  $(\text{C}_2\text{H}_5\text{OH}, 99\%)$  and  $(\text{CH}_4\text{N}_2\text{O}, 98\%)$ , were brought from Sigma Aldrich.

### 2.2 Sample preparation

#### 2.2.1 Fabrication of $\text{NiFe}_2\text{O}_4$

Flash auto-combustion was used to fabricate nickel ferrite nanoparticles. The starting concentrations of the precursors, such as nickel (0.1 M), and iron (0.2 M) nitrates, matched the specific ferrite's stoichiometric ratio. This precursor was combined with urea (0.7 M) through a powder phase; after

that, the resultant mixture was stirred vigorously while judicious drops of deionized water were incorporated to get the dissolved mixture. The nitrates: urea mixture was heated to  $250\text{ }^\circ\text{C}$  in order to start the process of breaking down the urea into ammonia, where ferrites could form. This equation could potentially be used to explain the following steps for the composition of  $\text{NiFe}_2\text{O}_4$ :



After the precipitation, the final powder has been calcined for 2 h at  $500\text{ }^\circ\text{C}$  at a rate of  $5\text{ }^\circ\text{C}/\text{min}$ .

#### 2.2.2 Preparation of $\text{TiO}_2$

$\text{TiO}_2$  nanoparticles were created by the sol–gel technique [38] by mixing 50 ml of an aqueous solution (25 ml deionized water, 25 ml ethanol) with 5 ml of Ti isopropoxide. After that, the mixture was continuously disturbed for thirty minutes. The final solution was then allowed to age for a full day. Subsequently, the precipitate was collected using a centrifuge and allowed to dry at  $50\text{ }^\circ\text{C}$ . Last but not least, the powder was calcined for two hours at  $550\text{ }^\circ\text{C}$  at a rate of  $5\text{ }^\circ\text{C}$  per minute.

#### 2.2.3 Synthesis of $\text{NiFe}_2\text{O}_4/\text{TiO}_2$ nanocomposite

Following these steps, a  $\text{NiFe}_2\text{O}_4/\text{TiO}_2$  nanocomposite was made with the same ratio. A 30-min ultrasonication process was used to combine 0.2 g of  $\text{NiFe}_2\text{O}_4$  with 50 ml of ethanol and water. Next, the mixture was subjected to a dropwise addition of 50 ml of Ti isopropoxide, followed by two hours of ultrasonication. and then aging for 24 h. Centrifugation was then used to separate the final product from the precipitate.  $\text{NiFe}_2\text{O}_4/\text{TiO}_2$  nanocomposite was obtained by heating the powder in a furnace for two hours at  $550\text{ }^\circ\text{C}$ .

### 2.3 Samples' analysis

Structural study has been achieved via X-ray diffractometer (using the Proker D8 advanced X-ray diffractometer, which has  $\text{CuK}\alpha$  radiation). Fourier-transform infrared spectroscopy (FT-IR) (Perkin Elmer) has been utilized to identify the function groups in range  $400\text{--}4000\text{ cm}^{-1}$ . The samples shape has been inspected through FESEM (field emission scanning electron microscopy) (Sigma 300VP operated at 15 kV) with Energy-dispersive X-ray (EDX). A UV–visible spectrophotometer (Jasco (V-630) spectrometer) has been utilized to investigate the optical properties of the obtained samples. Magnetic behaviors have been examined through VSM (Vibrating Sample Magnetometer, Lakeshore 7410S), in addition to a homemade device that measures

the magnetic susceptibility to various intensities of field. For the dielectric sample measurements, the powder was pressed in a uniaxial press at 5\*10<sup>8</sup> N/m<sup>2</sup> and coated with conducting silver paint at both surfaces to assure Ohmic contacts. Furthermore, dielectric properties related to the investigated samples were measured using the LCR bridge (HIOKI, 3532-50).

### 3 Results and discussion

Figure 1 shows the XRD of the investigated nanoparticles NiFe<sub>2</sub>O<sub>4</sub>, TiO<sub>2</sub> and their composite NiFe<sub>2</sub>O<sub>4</sub>/TiO<sub>2</sub>. According to ICDD card number 01-080-0072, NiFe<sub>2</sub>O<sub>4</sub> was prepared in a single phase cubic spinel structure. The diffraction peaks of NiFe<sub>2</sub>O<sub>4</sub> were observed at 2θ values 30.26°, 35.66°, 37.28°, 43.33°, 53.82°, 57.36°, 62.98°, 71.53°,

74.58°, and 75.53°, according to (220), (311), (222), (400), (422), (511), (440), (320), (533), and (622), respectively. The data for TiO<sub>2</sub> was indexed with the ICDD card number 01-076-1937. The main diffraction peak was observed at 2θ ≈ 25.307° corresponding to (210). The TiO<sub>2</sub> exhibited orthorhombic structure. The XRD pattern of the NiFe<sub>2</sub>O<sub>4</sub>/TiO<sub>2</sub> composite is shown in Fig. 1 and indicates the presence of two phases of NiFe<sub>2</sub>O<sub>4</sub> and TiO<sub>2</sub> simultaneously. The absence of a third phase approves the good physical mixing of compounds to form the nanocomposite without any chemical reactions. The lattice parameters of Ni ferrite were calculated according to the following equation based on the cubic structure:

$$\frac{1}{d^2} = (h^2 + k^2 + l^2) \frac{1}{a^2} \tag{1}$$

The lattice parameters of the orthorhombic TiO<sub>2</sub> were calculated from Eq. (2).

$$\frac{1}{d^2} = \frac{h^2}{a^2} + \frac{k^2}{b^2} + \frac{l^2}{c^2} \tag{2}$$

The lattice parameters of the investigated samples were reported in Table 1.

The crystallite sizes of NiFe<sub>2</sub>O<sub>4</sub>, TiO<sub>2</sub>, and NiFe<sub>2</sub>O<sub>4</sub>/TiO<sub>2</sub> were calculated using the well-known Scherer's equation: [39]

$$L = \frac{0.9\lambda}{\beta \cos\theta} \tag{3}$$

where L refers to the average crystallite size, λ denotes the wave length of the X-ray radiation (λ = 1.5406 Å), β is the corrected full width at half maximum intensity of the peak, and θ is the Bragg angle. Table 1 contains the values of the crystallite size of the investigated samples. Equation (4) was used to calculate the theoretical density (D<sub>x</sub>) of the investigated samples.

$$D_x = \frac{ZM}{N_A V} \tag{4}$$

where V is the unit cell volume, M denotes the molecular weight, Z is the number of molecules in a unit cell, and N<sub>A</sub> is Avogadro's number. The values of D<sub>x</sub> were reported in Table 1.

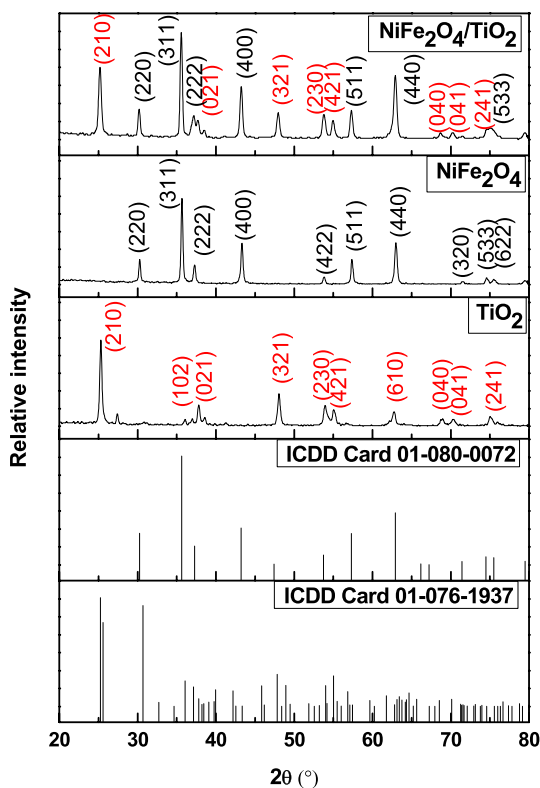


Fig. 1 XRD of the samples NiFe<sub>2</sub>O<sub>4</sub>, TiO<sub>2</sub> and NiFe<sub>2</sub>O<sub>4</sub>/TiO<sub>2</sub>

**Table 1** The lattice parameters, the theoretical density (D<sub>x</sub>), the dislocation density (δ) and the crystallite size of the samples NiFe<sub>2</sub>O<sub>4</sub>, TiO<sub>2</sub> and NiFe<sub>2</sub>O<sub>4</sub>/TiO<sub>2</sub>

Samples	a(Å)	b(Å)	c(Å)	L (nm)	D <sub>x</sub> (g/cm <sup>3</sup> )	δ × 10 <sup>-3</sup> (nm) <sup>-2</sup>
NiFe <sub>2</sub> O <sub>4</sub>	8.3480	8.3480	8.3480	48.3	5.3512	0.427
TiO <sub>2</sub>	9.5688	5.4666	5.1434	25.5	3.9428	1.530
NiFe <sub>2</sub> O <sub>4</sub> /TiO <sub>2</sub>	a for NiFe <sub>2</sub> O <sub>4</sub> 8.3665	b for NiFe <sub>2</sub> O <sub>4</sub> 8.3665	c for NiFe <sub>2</sub> O <sub>4</sub> 8.3665	32.4	4.6470	0.949
	a for TiO <sub>2</sub> 9.1793	b for TiO <sub>2</sub> 5.5433	c for TiO <sub>2</sub> 5.0398			

The dislocation density ( $\delta$ ) is related to the total defects in the samples and was calculated using Eq. (5) and listed in Table 1.

$$\delta = \frac{1}{L^2} \tag{5}$$

FTIR spectroscopy of  $\text{TiO}_2$ ,  $\text{NiFe}_2\text{O}_4$  and  $\text{NiFe}_2\text{O}_4/\text{TiO}_2$  nanocomposite was investigated. As revealed in Fig. 2, for the FTIR spectrum related to  $\text{NiFe}_2\text{O}_4$ , there are two noticeable absorption bands familiar to the spinel ferrite structure at  $433$  and  $620\text{ cm}^{-1}$  which are associated with the stretching vibration mode of the  $\text{M-O}$  bond at the octahedral in addition to tetrahedral sites correspondingly [40]. The band of absorption around  $1074\text{ cm}^{-1}$  was associated with a  $\text{Fe}^{3+}$  and  $\text{O}_2$  stretching vibration bond owing to existence of  $\text{Fe}^{3+}$  ions on the tetrahedral site according to the inverse spinel structure of  $\text{NiFe}_2\text{O}_4$  [41]. Furthermore, the band around  $1400\text{ cm}^{-1}$  was credited with  $-\text{CH}_2$  asymmetric band. In the  $\text{TiO}_2$  spectrum, the bands around  $568$  and  $901\text{ cm}^{-1}$  were corresponding to stretching vibration mode associated with  $\text{Ti-O-Ti}$  [42, 43]. For the FTIR spectra of  $\text{NiFe}_2\text{O}_4/\text{TiO}_2$  nanocomposite the distinctive bands of  $\text{NiFe}_2\text{O}_4$  and  $\text{TiO}_2$  approving the attendance of  $\text{NiFe}_2\text{O}_4$  and  $\text{TiO}_2$  NPs in nanocomposite. The absorption band around  $1630$  and  $3500\text{ cm}^{-1}$  was also associated with the  $\text{O-H}$  band, which is assigned to  $\text{O-H}$  bending as well as stretching vibrational modes owing to the adsorbed water molecule [44].

FESEM of the investigated samples is shown in Fig. 3. The FESEM image of the  $\text{NiFe}_2\text{O}_4$  is illustrated in Fig. 3a, and the particles have irregular shapes.  $\text{TiO}_2$  particles have spherical shapes, as illustrated in Fig. 3b. The shapes of the particles  $\text{NiFe}_2\text{O}_4$  and  $\text{TiO}_2$  are presented in Fig. 3c for the  $\text{NiFe}_2\text{O}_4/\text{TiO}_2$  nanocomposite.

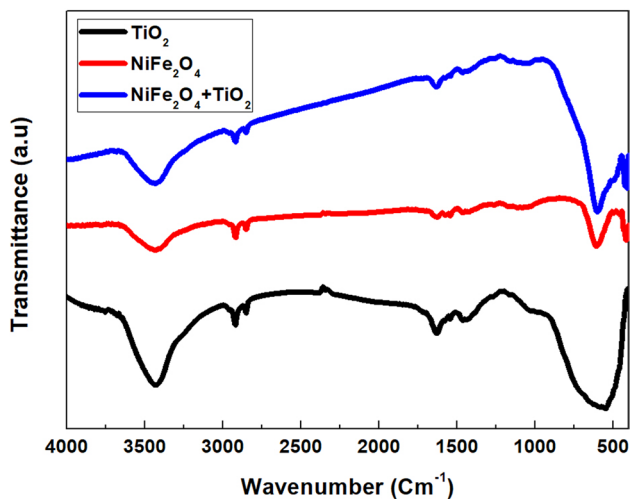


Fig. 2 FTIR of the prepared samples

Figure 4 illustrates the EDX of the investigated samples. The atomic % and weight % of the elements of the samples were illustrated in the inset tables in Fig. 4. The data obtained from the EDX illustrates that the investigated samples,  $\text{NiFe}_2\text{O}_4$ ,  $\text{TiO}_2$ , and  $\text{NiFe}_2\text{O}_4/\text{TiO}_2$ , were prepared with the same chemical formula. The presence of carbon elements in Fig. 4b is a result of the carbon tape where  $\text{TiO}_2$  was put on it inside the FESEM.

Figure 5 shows the absorbance of the UV-Vis. spectrum of  $\text{TiO}_2$ ,  $\text{NiFe}_2\text{O}_4$ , and  $\text{NiFe}_2\text{O}_4/\text{TiO}_2$  nanocomposite in the interior of  $200-1000\text{ nm}$ . According to this spectrum, all the samples absorb intensely the wavelengths of  $200-350\text{ nm}$  (ultraviolet light). By comparing the absorbance spectra of pure  $\text{TiO}_2$  and  $\text{NiFe}_2\text{O}_4$  NPs with  $\text{NiFe}_2\text{O}_4/\text{TiO}_2$  nanocomposite, there is a red shift. This indicates the complexation between  $\text{TiO}_2$  and  $\text{NiFe}_2\text{O}_4$  NPs. Figure 6a and b investigated the absorption coefficient ( $\alpha$ ) and extinction coefficient ( $K$ ) related to the prepared specimen and given through the ensuing equations [40].

$$\alpha = \frac{2.303A}{l} \tag{6}$$

$$K = \frac{\alpha\lambda}{4\pi} \tag{7}$$

where  $A$  is the absorbance,  $\lambda$  is wavelength, and  $l$  represents the specimen thickness.

Figure 6a. shows a clear peak around  $\lambda \approx 240\text{ nm}$  for all the prepared samples, which is related to  $\pi-\pi^*$  transitions [41]. Figure 6b shows a notable rise in the extinction coefficient ( $K$ ) of the investigated samples. The extinction coefficient gives information about the light portion that has been absorbed, scattered, or otherwise lost for every unit length of the dispersion medium.

Figure 7a and b displays Tauc plot for the direct and indirect transitions of  $\text{TiO}_2$ ,  $\text{NiFe}_2\text{O}_4$ , and  $\text{NiFe}_2\text{O}_4/\text{TiO}_2$  nanocomposite. The values of energy related to band gap were assumed from the Tauc relations, that have been calculated through these equations [42, 43]:

$$(\alpha h\nu)^2 = A(h\nu - E_g) \quad \text{On behalf of direct transitions} \tag{8}$$

$$(\alpha h\nu)^{0.5} = A(h\nu - E_g) \quad \text{On behalf of indirect transitions} \tag{9}$$

where  $A$ ,  $\alpha$  in addition to  $h\nu$  signify constants, absorption coefficient, and photon energy, respectively.

The energy band values of  $\text{TiO}_2$ ,  $\text{NiFe}_2\text{O}_4$ , and  $\text{NiFe}_2\text{O}_4/\text{TiO}_2$  nanocomposite are approximately  $3.4$ ,  $2.3$ , and  $2.5$ , respectively, for the indirect transition, which obviously reveals that the presence of  $\text{NiFe}_2\text{O}_4$  makes the  $\text{NiFe}_2\text{O}_4/\text{TiO}_2$  nanocomposite further sensitive to light than pure  $\text{TiO}_2$ . In light of the outcomes shown in Table 2, for values



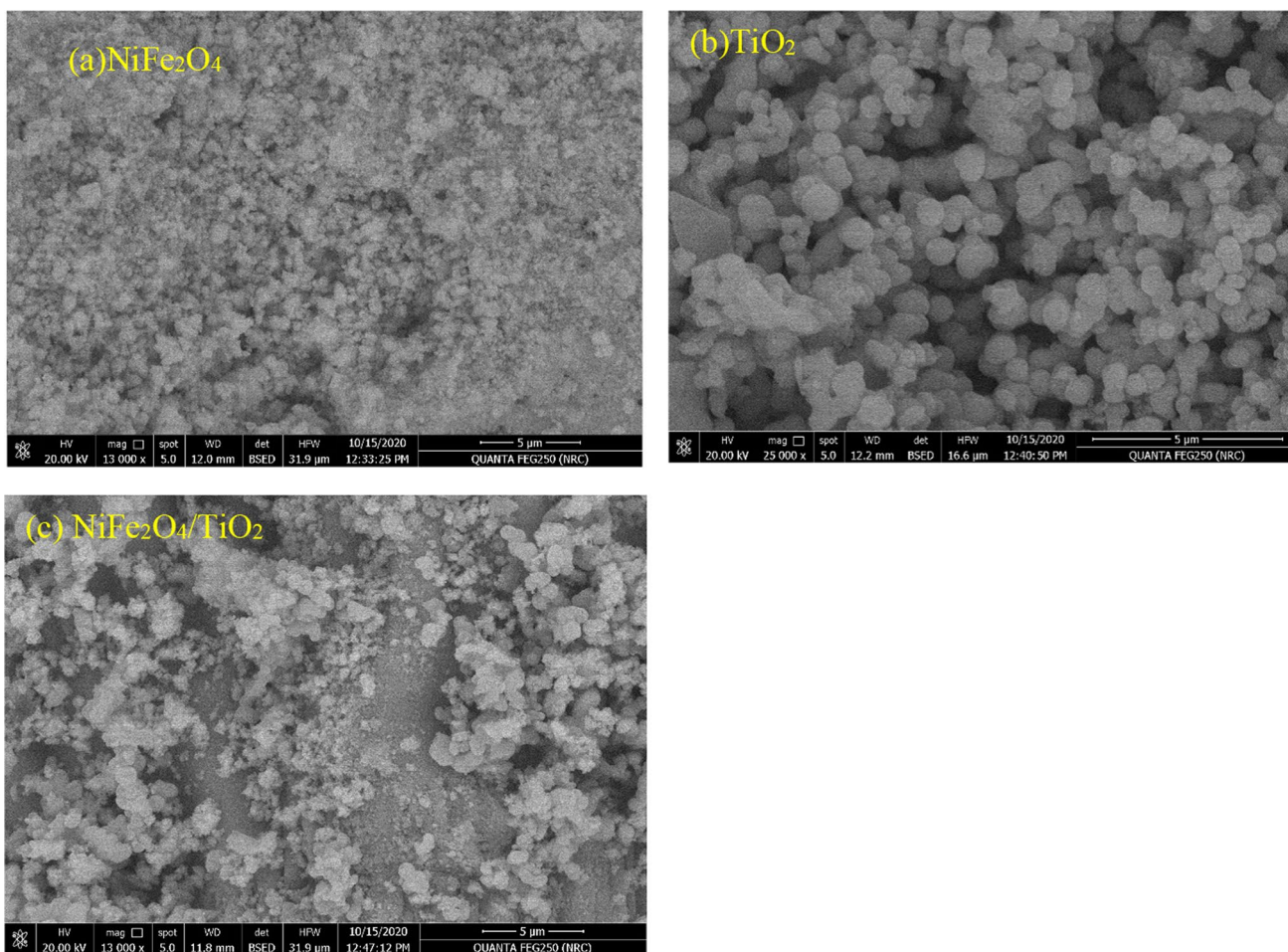


Fig. 3 FESEM of the samples a NiFe<sub>2</sub>O<sub>4</sub>, b TiO<sub>2</sub>, and c NiFe<sub>2</sub>O<sub>4</sub>/TiO<sub>2</sub>

related to direct and indirect energy band gap transitions, we noticed that the transition between valence and conduction bands associated with prepared samples follows indirect transitions.

Finally, based on the above argument, NiFe<sub>2</sub>O<sub>4</sub> nanoparticles have the capability of reducing the absorption edge related to TiO<sub>2</sub> in the visible light range, thus enhancing the photocatalytic performance of TiO<sub>2</sub> nanoparticles in the visible region.

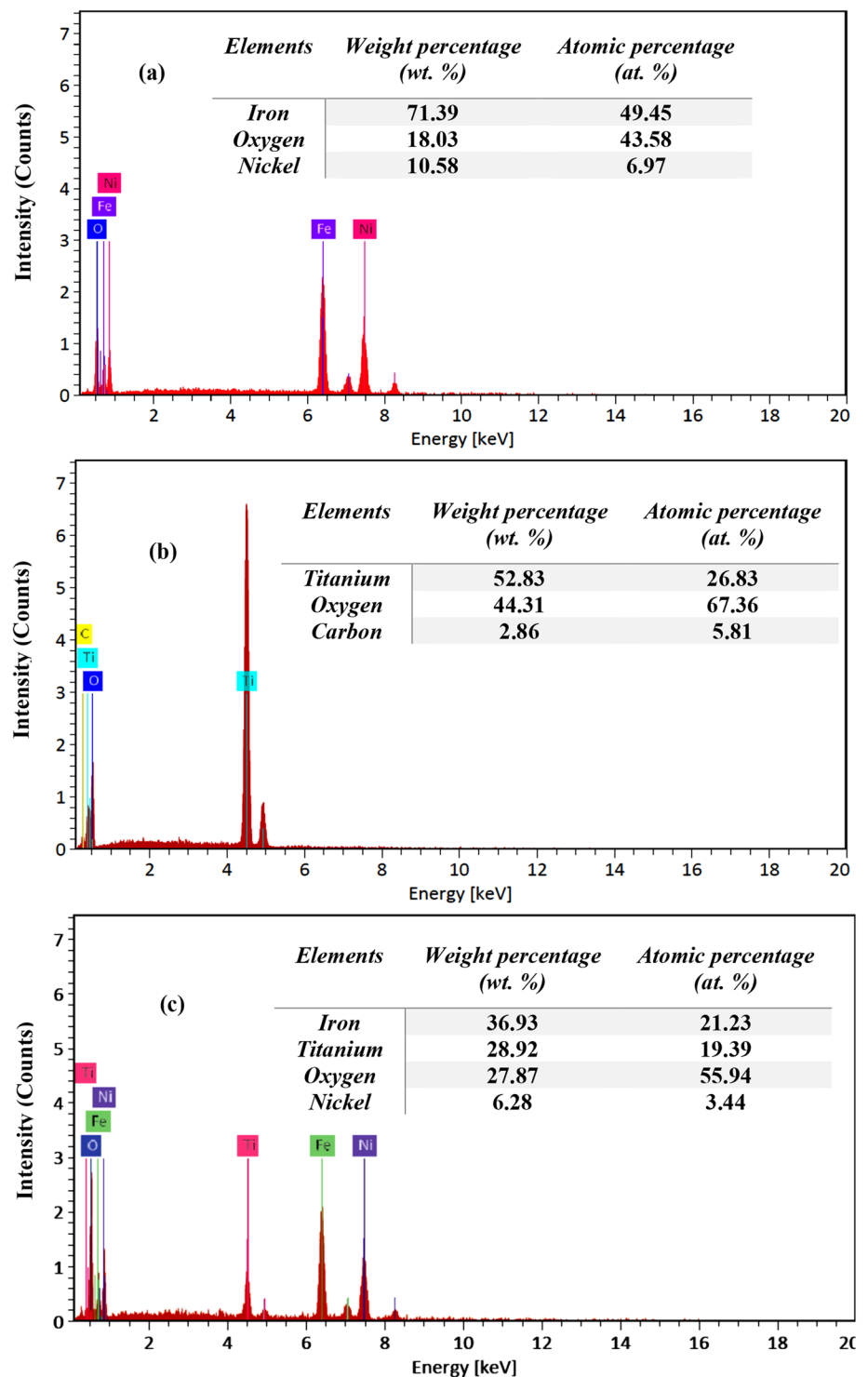
The value of the real dielectric constant ( $\epsilon'$ ) was calculated according to the following equation:

$$\epsilon' = \frac{Cd}{\epsilon_{oA}}, \tag{10}$$

where d refers to the thickness of the pellet, C is the capacitance of the sample, A is the pellet cross-sectional area and  $\epsilon_0$  is the permittivity in free space ( $\epsilon_0 = 8.86 \times 10^{-12}$  F/m).

Figure 8 illustrates the dependence of the dielectric constant ( $\epsilon'$ ) on the absolute temperature for NiFe<sub>2</sub>O<sub>4</sub>/TiO<sub>2</sub>. In the first temperature region (300–500 K),  $\epsilon'$  is nearly independent on the temperature. While in the second temperature region (500–600 K),  $\epsilon'$  increases with raising the temperature due to the sufficient thermal energy to liberate the dipoles to be aligned with the applied field, thereby the polarization and  $\epsilon'$  increased. Figure 8a shows that the correlation between the  $\epsilon'$  values and the frequency,  $\epsilon'$  decreases with increasing frequency. At very high frequencies, the electric dipoles are not able to follow the frequency of the applied field, so  $\epsilon'$  decreases. The dependence of the dielectric constant on the frequency originates from the presence of different types of polarization, such as ionic, space charge, electronic, and dipolar polarizations [45]. At low frequencies,  $\epsilon'$  values are high due to the participation of dipolar and space charge polarization. At high frequencies, the electronic and ionic

**Fig. 4** EDX of the samples **a** NiFe<sub>2</sub>O<sub>4</sub>, **b** TiO<sub>2</sub>, and **c** NiFe<sub>2</sub>O<sub>4</sub>/TiO<sub>2</sub>



polarization participate in the low dielectric constant. Space charge polarization is the result of charges being deposited at grain boundaries by an electric field applied at low frequencies. This results in a large number of capacitances, which

raise the dielectric constant. Because the charge exchange quickens in higher frequency regions, less polarization is obtained [46]. As a result, the dielectric constant values are reduced and almost constant. The comparative study of

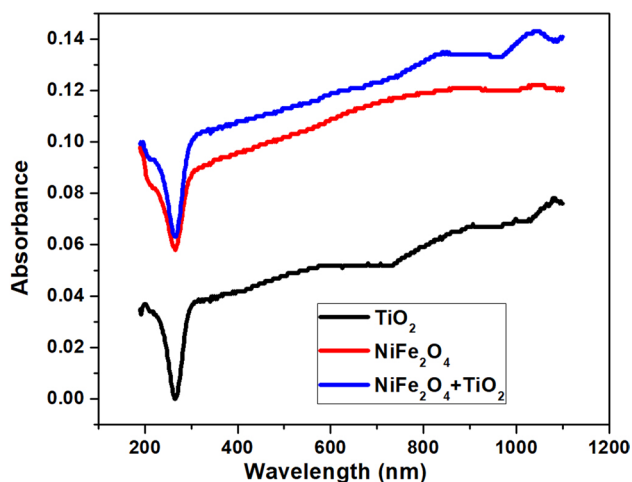


**Fig. 5** Absorbance of UV-Vis spectrum of TiO<sub>2</sub>, NiFe<sub>2</sub>O<sub>4</sub>, in addition to NiFe<sub>2</sub>O<sub>4</sub>/TiO<sub>2</sub>

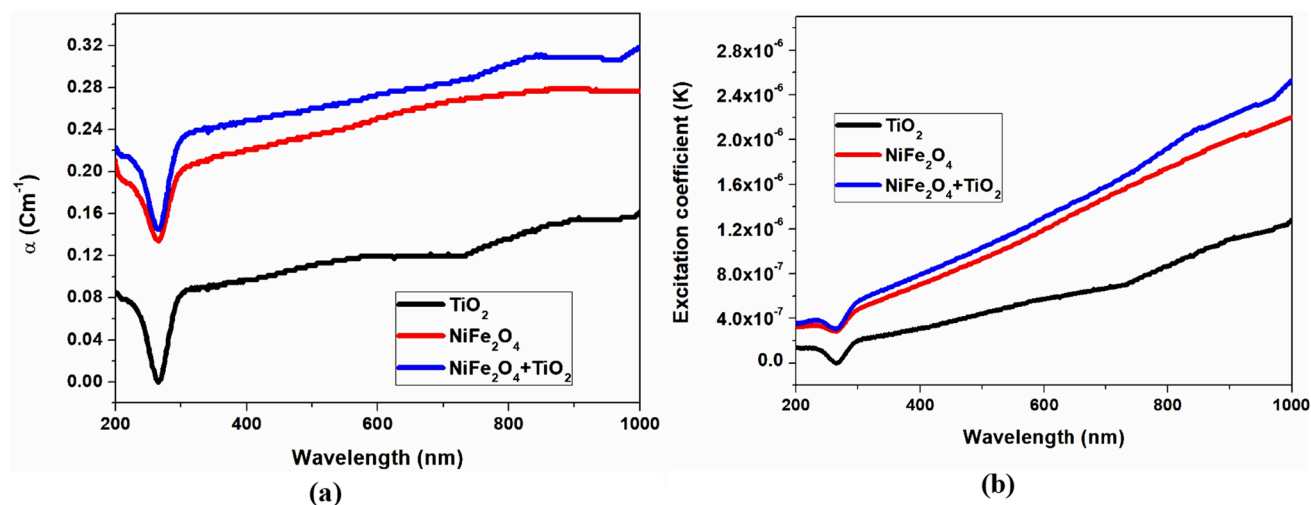
$\epsilon'$  and T(K) for the samples NiFe<sub>2</sub>O<sub>4</sub> and NiFe<sub>2</sub>O<sub>4</sub>/TiO<sub>2</sub> is shown in Fig. 8b. It was observed that the  $\epsilon'$  values of NiFe<sub>2</sub>O<sub>4</sub>/TiO<sub>2</sub> is larger than that of pure NiFe<sub>2</sub>O<sub>4</sub>. The presence of TiO<sub>2</sub> in the NiFe<sub>2</sub>O<sub>4</sub>/TiO<sub>2</sub> increases the dielectric constant due to enhancement of the polarization from the conduction mechanism as a result of the charges hopping between various ions leading to the increase in the space charge polarization [45]. Moreover, the interfacial polarization is initiated the interfaces between grain of different compositions of the nanocomposite.

Figure 9 shows the dependence of ac conductivity on the reciprocal of T for the composite NiFe<sub>2</sub>O<sub>4</sub>/TiO<sub>2</sub>. The investigated samples have a semiconductor like behavior due to the ac conductivity increases with raising the temperature. The values of  $\sigma_{ac}$  obey the Arrhenius equation [44]:

$$\sigma = \sigma_0 \exp \frac{-E}{kT}, \tag{11}$$

where T denotes the absolute temperature, E refers to the activation energy, and k is the Boltzmann's constant. The values of the activation energies were calculated and reported in Table 3. The values of activation energies indicate the semiconductor like behavior. The values of E of NiFe<sub>2</sub>O<sub>4</sub>/TiO<sub>2</sub> composite are less than that of Ni ferrite due to the presence of semiconductor TiO<sub>2</sub> particles. The NiFe<sub>2</sub>O<sub>4</sub>/TiO<sub>2</sub> sample exhibits an increase in ac conductivity due to an increase in space charge carriers and their mobility. The decrease in the activation energy of the NiFe<sub>2</sub>O<sub>4</sub>/TiO<sub>2</sub> composite recommends the use of these materials in heavy metal photodegradation.

The variation of the molar magnetic susceptibility ( $\chi_M$ ) with T at different magnetic field intensities (H = 1010 Oe, 1340 Oe, and 1660 Oe) for NiFe<sub>2</sub>O<sub>4</sub> and NiFe<sub>2</sub>O<sub>4</sub>/TiO<sub>2</sub> composite is shown in Fig. 10a and b. A sensible decrease in ( $\chi_M$ ) with increasing temperature is detected until a certain temperature (T<sub>c</sub>) after which it reaches its minimum value. The inset of the figure shows  $\delta\chi_M/\delta T$  from which the Curie temperature T<sub>c</sub> is depicted.



**Fig. 6** **a** Absorption coefficient and **b** Extinction coefficient of TiO<sub>2</sub>, NiFe<sub>2</sub>O<sub>4</sub>, and NiFe<sub>2</sub>O<sub>4</sub>/TiO<sub>2</sub> nanocomposite

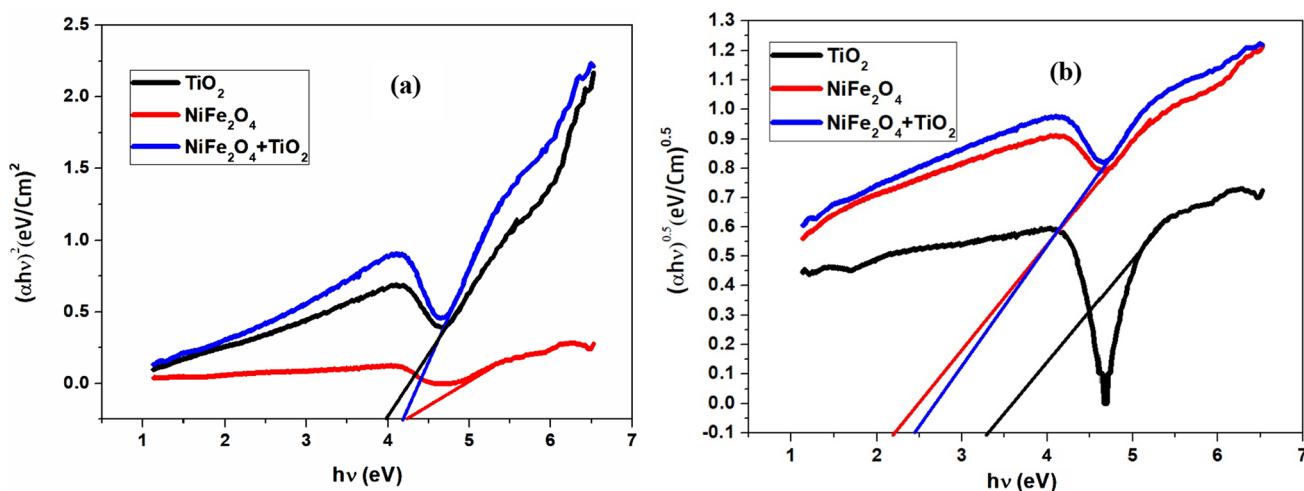


Fig. 7 a Direct and b indirect transition of TiO<sub>2</sub>, NiFe<sub>2</sub>O<sub>4</sub>, and NiFe<sub>2</sub>O<sub>4</sub>/TiO<sub>2</sub> nanocomposite

Table 2 Values of direct and indirect band gap transition energies of TiO<sub>2</sub>, NiFe<sub>2</sub>O<sub>4</sub>, and NiFe<sub>2</sub>O<sub>4</sub>/TiO<sub>2</sub> nanocomposite

Sample	E <sub>g</sub> (direct) (eV)	E <sub>g</sub> (indirect) (eV)
TiO <sub>2</sub>	4.25	3.4
NiFe <sub>2</sub> O <sub>4</sub>	4	2.3
NiFe <sub>2</sub> O <sub>4</sub> /TiO <sub>2</sub>	4.2	2.5

From Fig. 10C, it was obvious that the molar magnetic susceptibility ( $\chi_M$ ) of nanocomposite is smaller than that of Ni ferrite. On the other hand, both effective moments and

Curie temperatures for the nanocomposite were larger than for the pure nano Ni ferrite.

The Curie–Weiss law [40] was for compliance at the high-temperature region. Accordingly, the Curie temperature ( $T_c$ ), Curie–Weiss constant ( $\theta$ ), and the effective magnetic moment ( $\mu_B$ ) are detected from the paramagnetic region of the relation between  $\chi^{-1}_M$  and absolute temperature (not present here) by applying the subsequent formulas [47]. Table 4 tabulates the computed data.

$$C = 1/\text{slope} \quad \mu_{\text{eff}} = 2.83\sqrt{C}. \tag{12}$$

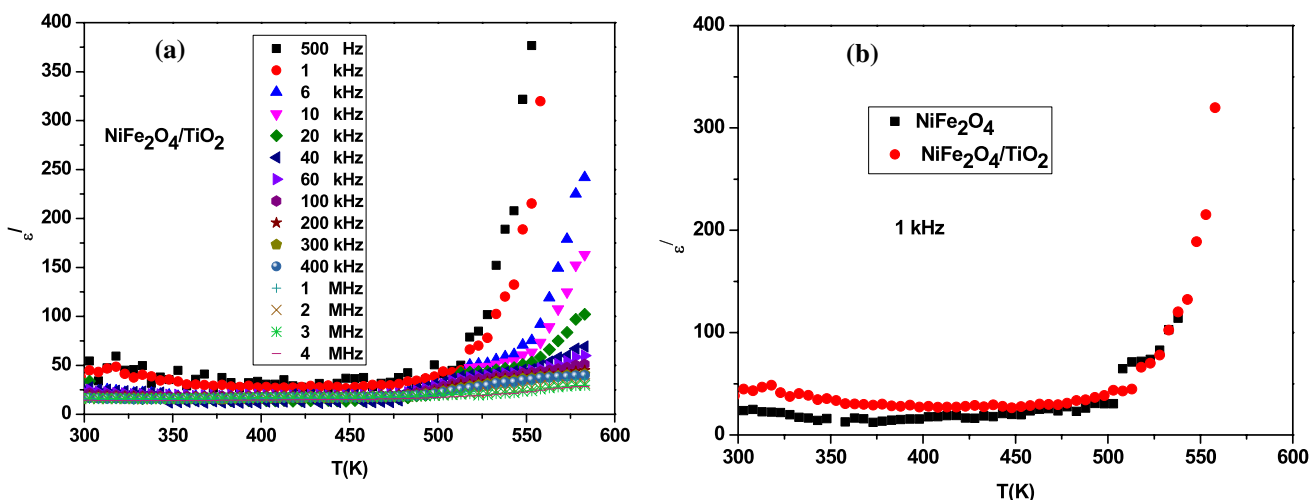
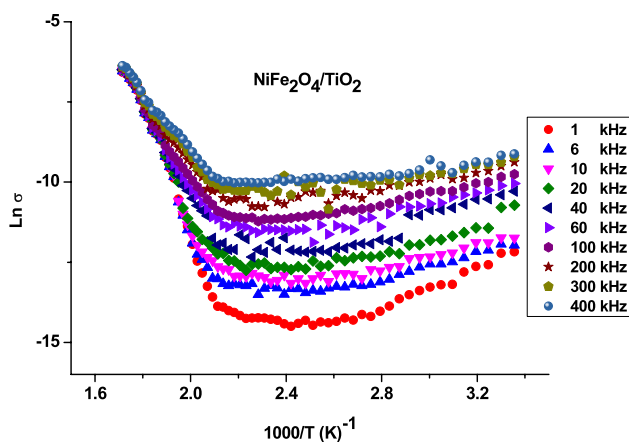


Fig. 8 a The dependence of  $\epsilon'$  on the absolute temperature. b A comparative study of  $\epsilon'$  for NiFe<sub>2</sub>O<sub>4</sub> and NiFe<sub>2</sub>O<sub>4</sub>/TiO<sub>2</sub> as a function of temperature





**Fig. 9** The relation between ac conductivity and the reciprocal of absolute temperature for the composite NiFe<sub>2</sub>O<sub>4</sub>/TiO<sub>2</sub> at different frequencies

**Table 3** The values of activation energies E<sub>I</sub> (at high temperature region) and E<sub>II</sub> (at low temperature region) for the samples

Frequency	NiFe <sub>2</sub> O <sub>4</sub>		NiFe <sub>2</sub> O <sub>4</sub> /TiO <sub>2</sub>	
	E <sub>I</sub> (eV)	E <sub>II</sub> (eV)	E <sub>I</sub> (eV)	E <sub>II</sub> (eV)
10 kHz	2.60	1.45	0.94	0.93
100 kHz	1.12	0.62	1.17	0.91
400 kHz	0.94	0.74	0.85	0.69

The tabulated data shows that the Curie temperature T<sub>c</sub> decreases as TiO<sub>2</sub> is added to the pure Ni ferrite, but the effective magnetic moment (μ<sub>B</sub>) increases.

The value of T<sub>c</sub> represents the strength of characteristic magnetic interactions, i.e., A-B exchange interactions, between the cations present at the tetrahedral and octahedral lattice sites in Ni ferrite, so the thermal energy required to regulate the spin alignment decreases, thus decreasing the Curie temperature [48, 49] due to weakness in the A-B exchange interaction as TiO<sub>2</sub> was added.

The composite has a ferrimagnetic nature at room temperature, it can be described by a model of indirect double exchange, which is explained by oxygen vacancies and the exchange interaction between the 3d orbitals of Ti<sup>3+</sup> and Ti<sup>4+</sup> at the interface [42].

The magnetic hysteresis curves at 300 K are typical of ferrimagnetic materials. In general, the shape and width of the hysteresis loop depend on some factors, such as

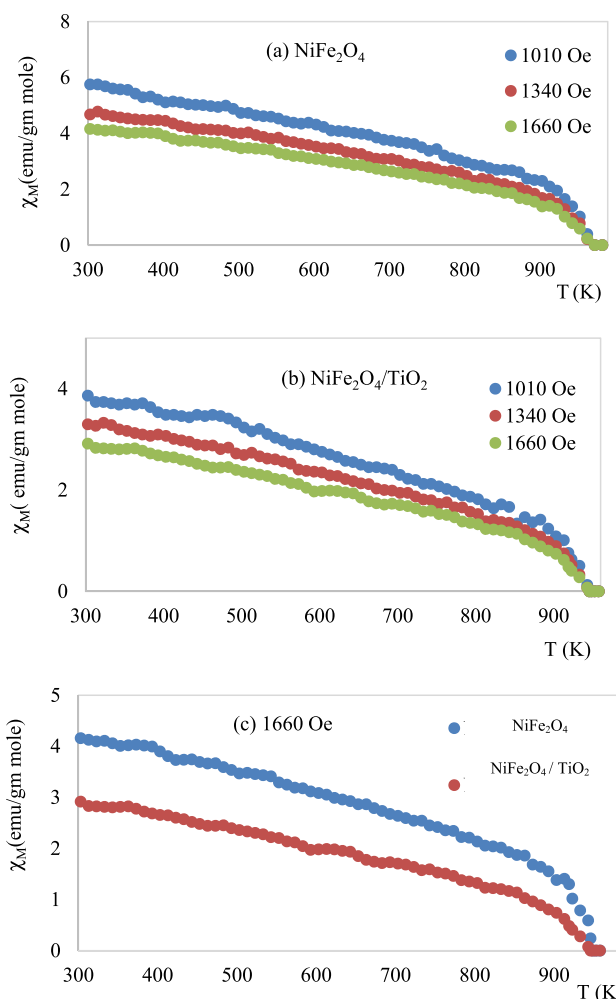


**Fig. 10** a, b Variation of χ<sub>M</sub> with the absolute temperature T at different magnetic field intensities. c Variation of χ<sub>M</sub> for pure Ni ferrite and its composite with the absolute temperature T at 1660 Oe

**Table 4** Shows the Curie temperature T<sub>c</sub>, Weiss constant (θ), and the effective magnetic moment (μ<sub>B</sub>) for our samples

Sample	magnetic field (Oe)	T <sub>c</sub> (K)	θ (K)	μ <sub>eff</sub> (B.M)
NiFe <sub>2</sub> O <sub>4</sub>	1010	963	936	9.43
	1340	963	934	6.69
	1660	963	932	5.92
NiFe <sub>2</sub> O <sub>4</sub> /TiO <sub>2</sub>	1010	923	912	13.03
	1340	923	913	8.94
	1660	923	909	8.58

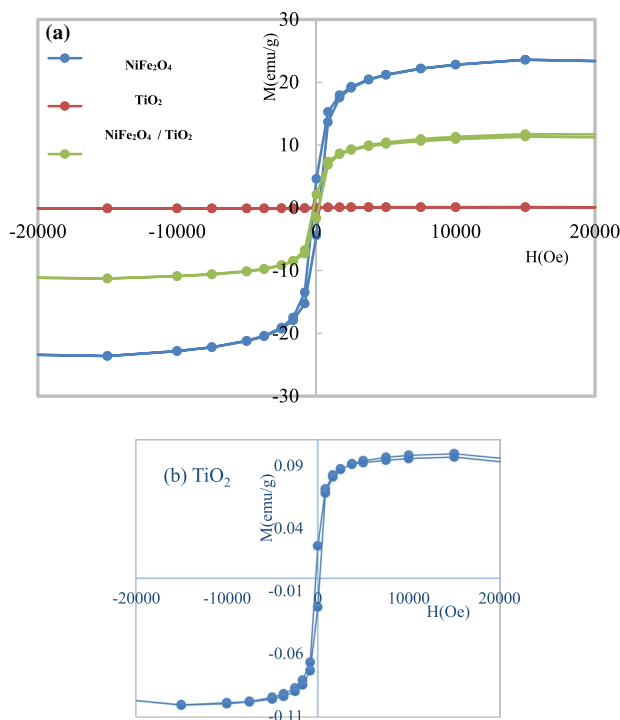


**Fig. 11** a, b Illustrates magnetization versus external magnetic field steps are not monotonic

chemical composition, cation distribution, porosity, grain size, etc. Figure 11a and b illustrates the magnetization versus external magnetic field ( $M$ – $H$ ) hysteresis loop which is determined with an external applied magnetic field ranging between  $-20$  and  $20$  kOe. the  $M_s$  value that corresponds to  $20$  kOe is  $23.604$  emu/g.

From the hysteresis loop,  $M_s$ , remnant magnetization ( $M_r$ ),  $H_c$ , squareness ( $M_r/M_s$ ), experimental magnetic moments ( $n_B$ ), and anisotropy constant ( $K$ ) are illustrated in Table 5.

Stoner–Wohlfarth relation were used to calculate the anisotropy constant ‘ $K$ ’ as follows [50]:

$$K = \frac{H_C \times M_S}{0.96} \quad (13)$$

**Table 5** Shows the saturation magnetization ( $M_s$ ), remnant magnetization ( $M_r$ ), coercivity ( $H_c$ ), squareness ( $M_r/M_s$ ), experimental magnetic moments ( $n_B$ ), and anisotropy constant ( $K$ )

Sample	$M_s$ (emu/g)	$M_r$ (emu/g)	$H_c$ (Oe)	$M_r/M_s$	$n_B$ (exp) ( $\mu_B$ )	$K$ (Oe. emu/g $\times 10^3$ )
NiFe <sub>2</sub> O <sub>4</sub>	23.604	4.505	207.92	0.191	0.99	5.008
TiO <sub>2</sub>	$9.97 \times 10^{-2}$	$2.42 \times 10^{-2}$	220.79	0.243	0.001	0.023
NiFe <sub>2</sub> O <sub>4</sub> /TiO <sub>2</sub>	11.502	1.8732	180.19	0.163	0.647	2.115

At room temperature, the experimental magnetic moment  $n_B$  is calculated from the saturation magnetization ( $M_s$ ) value as mentioned in the previous work [47, 51] as follows:

$$n_B = \frac{M_w \times M_s}{5585} \quad (14)$$

The table makes it evident that the magnetic parameters of the NiFe<sub>2</sub>O<sub>4</sub>/TiO<sub>2</sub> composite have lower values compared with the pure nanoferrite sample. The lower value of saturation magnetization could result from the existence of spin canting, which was reported in several nanometer-sized [52] in addition to the frustrated spin structure at the interfaces. Since the squareness ratio  $< 0.5$  is mostly ascribed to the formation of a multi-domain MD structure, then ( $M_r/M_s$ ) values refer to the particles interact by magneto static interactions ( $M_r/M_s < 0.5$ ), comparison with the reported literature will be an added value, especially for the room temperature parameters.

## 4 Conclusion

Flash combustion synthesis was used to prepare nanoparticles of NiFe<sub>2</sub>O<sub>4</sub>, while TiO<sub>2</sub> nanoparticles were synthesized using sol–gel method. The nanocomposite magnetic catalyst obtained from a combination between both NiFe<sub>2</sub>O<sub>4</sub> and TiO<sub>2</sub> nanoparticles. Results from FESEM, FTIR, and XRD show that TiO<sub>2</sub> and NiFe<sub>2</sub>O<sub>4</sub> NPs were successfully synthesized. The NiFe<sub>2</sub>O<sub>4</sub>/TiO<sub>2</sub> composite's XRD pattern is depicted and demonstrates the simultaneous existence of two phases, NiFe<sub>2</sub>O<sub>4</sub> and TiO<sub>2</sub>. From the optical study, we concluded that the addition of NiFe<sub>2</sub>O<sub>4</sub> makes the nanocomposite more sensitive to light than pure TiO<sub>2</sub>. As the value of  $E_g$  decreased from  $3.4$  to  $2.5$  eV, and the activation energy of the NiFe<sub>2</sub>O<sub>4</sub>/TiO<sub>2</sub> nanocomposite reached  $0.85$  and  $0.69$  at  $400$  kHz, we recommended the use of these materials in heavy metal photodegradation. The magnetic hysteresis curves at  $300$  K are typical of ferrimagnetic materials for NiFe<sub>2</sub>O<sub>4</sub> and its nanocomposite with TiO<sub>2</sub>. This pointed to the facility of reuse this catalyst after magnetic decantation of treated water.

**Author contributions** Dalia N. Ghaffar: Methodology, and written the manuscript. M. M. Arman: Methodology and write the manuscript. S.I. El-Dek Preparation of the samples, and write the manuscript. Rania Ramadan: Preparation of the samples, and write the manuscript.

**Funding** Open access funding provided by The Science, Technology & Innovation Funding Authority (STDF) in cooperation with The Egyptian Knowledge Bank (EKB).

**Data availability** The data are available upon request.

## Declarations

**Conflict of interest** The authors declare that they have no conflict of interest.

**Open Access** This article is licensed under a Creative Commons Attribution 4.0 International License, which permits use, sharing, adaptation, distribution and reproduction in any medium or format, as long as you give appropriate credit to the original author(s) and the source, provide a link to the Creative Commons licence, and indicate if changes were made. The images or other third party material in this article are included in the article's Creative Commons licence, unless indicated otherwise in a credit line to the material. If material is not included in the article's Creative Commons licence and your intended use is not permitted by statutory regulation or exceeds the permitted use, you will need to obtain permission directly from the copyright holder. To view a copy of this licence, visit <http://creativecommons.org/licenses/by/4.0/>.

## References

1. A. M. El-Sayed, *Mater. Chem. Phys.* **82**, 583–587 (2003)
2. S.N.A. Hussain, *Opt. Mater.* **139**, 113797 (2023)
3. A. Azizi, J. Saien, Optimization of Cr(VI) photocatalytic reduction by UV/TiO<sub>2</sub>: influence of inorganic and organic species and kinetic study. *Arch Hyg Sci* **7**(2), 81–90 (2018)
4. S. Bakardjieva, J. Subrt, V. Stengl, M.J. Dianez, M.J. Sayagues, Photoactivity of anatase–rutile TiO<sub>2</sub> nanocrystalline mixtures obtained by heat treatment of homogeneously precipitated anatase. *Appl. Catal. B* **58**, 193–202 (2005)
5. S. Chandrasekaran, C. Bowen, P. Zhang, Z. Li, Q. Yuan, X. Ren, L. Deng, Spinel photocatalysts for environmental remediation, hydrogen generation, CO<sub>2</sub> reduction and photoelectrochemical water splitting. *J. Mater. Chem. A* **6**, 11078 (2018)
6. C.J. Chang, Z. Lee, M.D. Wei, C.C. Chang, K.W. Chu, Photocatalytic hydrogen production by magnetically separable Fe<sub>3</sub>O<sub>4</sub>@ ZnS and NiCo<sub>2</sub>O<sub>4</sub>@ ZnS core-shell nanoparticles. *Int. J. Hydrogen Energy* **40**(35), 11436–11443 (2015)
7. C.J. Chang, Z. Lee, K.W. Chu, Y.H. Wei, Chang, CoFe<sub>2</sub>O<sub>4</sub>@ ZnS core-shell spheres as magnetically recyclable photocatalysts for hydrogen production. *J. Taiwan Inst. Chem. Eng.* **66**, 386–393 (2016)
8. Z. Duan, Y. Zhu, Z. Hub, J. Zhang, D. Liu, X. Luo, M. Gao, L. Lei, X. Wang, G. Zhao, Micro-patterned NiFe<sub>2</sub>O<sub>4</sub>/Fe–TiO<sub>2</sub> composite films: fabrication, hydrophilicity and application in visible-light-driven photocatalysis. *Ceram. Int.* **46**, 27080–27091 (2020)
9. P. Laokul, V. Amornkitbamrung, S. Seraphin, S. Maensiri, Characterization and magnetic properties of nanocrystalline CuFe<sub>2</sub>O<sub>4</sub>, NiFe<sub>2</sub>O<sub>4</sub>, ZnFe<sub>2</sub>O<sub>4</sub> powders prepared by the Aloe vera extract solution. *Curr. Appl. Phys.* **11**(1), 101–108 (2011)
10. O. Kerkez-Kuyumcu, E. Kibar, K. Dayıoğlu, F. Gedik, A.N. Akın, Ş. Özkara-Aydınoğlu, A comparative study for removal of different dyes over M/TiO<sub>2</sub> (M = Cu, Ni Co, Fe, Mn and Cr) photocatalysts under visible light irradiation. *J. Photochem. Photobiol. A* **311**, 176–185 (2015)
11. X. Zhu, F. Zhang, M. Wang, J. Ding, S. Sun, J. Bao, C. Gao, Facile synthesis, structure and visible light photocatalytic activity of recyclable ZnFe<sub>2</sub>O<sub>4</sub>/TiO<sub>2</sub>. *Appl. Surf. Sci.* **319**, 83–89 (2014)
12. G. Rekhila, Y. Bessekhoud, M. Trari, Visible light hydrogen production on the novel ferrite NiFe<sub>2</sub>O<sub>4</sub>. *Int. J. Hydrog. Energy* **38**, 6335–6343 (2013)
13. P. Sathishkumar, R.V. Mangalaraja, S. Anandan, M. Ashokkumar, CoFe<sub>2</sub>O<sub>4</sub>/TiO<sub>2</sub> nanocatalysts for the photocatalytic degradation of Reactive Red 120 in aqueous solutions in the presence and absence of electron acceptors. *Chem. Eng. J.* **220**, 302–310 (2013)
14. P.A.K. Reddy, S. Basavaraju, D.K. Valluri, V.S. Muthukonda, S. Machiraju, J.S. Lee, CaFe<sub>2</sub>O<sub>4</sub> sensitized hierarchical TiO<sub>2</sub> photo composite for hydrogen production under solar light irradiation. *Chem. Eng. J.* **247**, 152–160 (2014)
15. C. Peng, W. Fan, Q. Li, W. Han, X. Chen, G. Zhang, Y. Yan, Q. Gu, C. Wang, H. Zhang et al., Boosting photocatalytic activity through tuning electron spin states and external magnetic fields. *J. Mater. Sci. Technol.* **115**, 208–220 (2022). <https://doi.org/10.1016/j.jmst.2021.11.031>
16. N. Li, M. He, X. Lu, L. Liang, R. Li, B. Yan, G. Chen, Enhanced norfloxacin degradation by visible-light-driven Mn<sub>3</sub>O<sub>4</sub>/γ-MnOOH photocatalysis under weak magnetic field. *Sci. Total. Environ.* **761**, 143268 (2021). <https://doi.org/10.1016/j.scitotenv.2020.143268>
17. J. Li, Q. Pei, R. Wang, Y. Zhou, Z. Zhang, Q. Cao, D. Wang, W. Mi, Y. Du, Enhanced photocatalytic performance through magnetic field boosting carrier transport. *ACS Nano* **12**, 3351–3359 (2018). <https://doi.org/10.1021/acs.nano.7b08770>
18. Y. Wang, S. Wang, Y. Wu, Z. Wang, H. Zhang, Z. Cao, J. He, W. Li, Z. Yang, L. Zheng et al., A α-Fe<sub>2</sub>O<sub>3</sub>/rGO magnetic photocatalyst: enhanced photocatalytic performance regulated by magnetic field. *J. Alloy. Compd.* **851**, 156733 (2021). <https://doi.org/10.1016/j.jallcom.2020.156733>
19. Y.M. Hao, C. Man, Z.B. Hu, Effective removal of Cu (II) ions from aqueous solution by amino-functionalized magnetic nanoparticles. *J. Hazard. Mater.* **184**, 392–399 (2010). <https://doi.org/10.1016/j.jhazmat.2010.08.048>
20. L. Zhang, Y. He, Y. Wu, T. Wu, Photocatalytic degradation of RhB over MgFe<sub>2</sub>O<sub>4</sub>/TiO<sub>2</sub> composite materials. *Mater. Sci. Eng. B* **176**, 1497–1504 (2011)
21. Y. Lu, H.-C. Wang, X. She, D. Huang, Y. Yang, X. Gao, Z. Zhu, X. Liu, Z. Xie, A novel preparation of GO/NiFe<sub>2</sub>O<sub>4</sub>/TiO<sub>2</sub> nanorod arrays with enhanced photocatalytic activity for removing unsymmetrical dimethylhydrazine from water. *Mater. Sci. Semicond. Process.* **121**, 105448 (2021)
22. P. Cheng, C. Deng, M. Gu, W. Shangguan, Visible-light responsive zinc ferrite doped titania photocatalyst for methyl orange degradation. *J. Mater. Sci.* **42**, 9239–9244 (2007)
23. M.M. Arman, Preparation, characterization and magnetic properties of Sm<sub>0.95</sub>Ho<sub>0.05</sub>FeO<sub>3</sub> nanoparticles and their application in the purification of water. *Appl. Phys. A* **129**(1), 38 (2023)
24. Lu. Ya-bo, H.-C. Wang, X.-Y. She, D. Huang, Y.-X. Yang, X. Gao, Z.-M. Zhu, X.-X. Liu, Z. Xie, A novel preparation of GO/NiFe<sub>2</sub>O<sub>4</sub>/TiO<sub>2</sub> nanorod arrays with enhanced photocatalytic activity for removing unsymmetrical dimethylhydrazine from water. *Mater. Sci. Semicond. Process.* **121**, 105448 (2021)
25. Y. Abbas, I.S. Han, A.S. Sokolov, Y.R. Jeon, C. Choi, Rapid thermal annealing on the atomic layer-deposited zirconia thin film to enhance resistive switching characteristics. *J. Mater. Sci. Mater. Electron.* **31**, 903–909 (2020)
26. H. Abbas, M.R. Park, Y. Abbas, Q. Hu, T.S. Kang, T.S. Yoon, C.J. Kang, Resistive switching characteristics of manganese oxide

- thin film and nanoparticle assembly hybrid devices. *Jpn. J. Appl. Phys.* **57**, 06HC03 (2018)
27. Y. Abbas, S.M. Ansari, I. Taha, H. Abunahla, M.U. Khan, M.D. Rezeq, H.M. Aldosari, B. Mohammad, Stopping voltage-dependent PCM and RRAM-based neuromorphic characteristics of germanium telluride *Adv. Funct. Mater.* **33**, 2214615 (2023)
  28. Y. Abbas, R.B. Ambade, S.B. Ambade, T.H. Han, C. Choi, Tailored nanoplateau and nanochannel structures using solution-processed rutile TiO<sub>2</sub> thin films for complementary and bipolar switching characteristics. *Nanoscale* **11**, 13815–13823 (2019)
  29. N.A. Ahir, A.V. Takaloo, K.A. Nirmal, S.S. Kundale, M.Y. Chougale, J. Bae, D. Kim, T.D. Dongale, *Mater. Sci. Semicond. Process. Semicond. Process.* **125**, 105646 (2021)
  30. C. Hu, M. McDaniel, A. Posadas, A. Demkov, J. Ekerdt, E. Yu, Highly controllable and stable quantized conductance and resistive switching mechanism in single-crystal TiO<sub>2</sub> resistive memory on silicon. *Nano Lett.* **14**, 4360–4367 (2014)
  31. O. Krestinskaya, A. Irmanova and A. P. James, Memristors: properties, models, materials. *Deep learning classifiers with memristive Networks. Modeling and Optimization in Science and Technologies*, vol. 14 (Switzerland: Springer, Cham) pp. 13–40 (2020)
  32. F. Gul, H. Efeoglu, Bipolar resistive switching and conduction mechanism of an Al/ZnO/Al-based memristor. *Superlattices Microstruct. Microstruct.* **101**, 172–179 (2017)
  33. A.S. Nikam, G.U. Kamble, A.R. Patil, S.B. Patil, A.D. Sheikh, A.V. Takaloo, P.K. Gaikwad, R.K. Kamat, J.H. Kim, T.D. Dongale, *Nanotechnology* **34**, 425201 (2023)
  34. Y.S. Lin, F. Zeng, S.G. Tang, H.Y. Liu, C. Chen, S. Gao, Y.G. Wang, F. Pan, Resistive switching mechanisms relating to oxygen vacancies migration in both interfaces in Ti/HfOx/Pt memory devices. *J. Appl. Phys.* **113**, 064510 (2013)
  35. Y. Abbas, Y.R. Jeon, A.S. Sokolov, S. Kim, B. Ku, C. Choi, Compliance-free, digital SET and analog RESET synaptic characteristics of sub-tantalum oxide based neuromorphic device. *Sci. Rep.* **8**, 1228 (2018)
  36. H.L. Park, T.W. Lee, Organic and perovskite memristors for neuromorphic computing. *Org. Electron.* **98**, 106301 (2021)
  37. R.P. Patil, A.S. Nikam, S.B. Teli, A.V. Takaloo, R.K. Kamat, T.D. Dongale, P.D. Kamble, K.M. Garadkar, *Semicond. Sci. Technol.* **38**, 125002 (2023)
  38. M.V. Arularasu, Effect of organic capping agents on the optical and photocatalytic activity of mesoporous TiO<sub>2</sub> nanoparticles by sol–gel method. *SN Appl. Sci.* **1**, 393 (2019)
  39. E.E. Ateia, D. Gawad, M.M. Arman, Ab-initio study of structural, morphological and optical properties of multiferroic La<sub>2</sub>FeCrO<sub>6</sub>. *J. Alloy. Compd.* **976**, 173017 (2024)
  40. A.Z. Saravani, M. Nadimi, M.A. Aroon, A.E. Pirbazari, Magnetic TiO<sub>2</sub>/NiFe<sub>2</sub>O<sub>4</sub>/reduced graphene oxide nanocomposite as a recyclable photocatalyst for photocatalytic removal of methylene blue under visible light. *J. Alloy. Compd.* **803**, 291–306 (2019)
  41. A.M. Ismail, R. Ramadan, M.M. El-Masry, The role of nanoparticles inclusion in monitoring the physical properties of PVDF. *J. Aust. Ceramic Soc.* (2023). <https://doi.org/10.1007/s41779-023-00836-4>
  42. M.M. El-Masry, R. Ramadan, The effect of CoFe<sub>2</sub>O<sub>4</sub>, CuFe<sub>2</sub>O<sub>4</sub> and Cu/CoFe<sub>2</sub>O<sub>4</sub> nanoparticles on the optical properties and piezoelectric response of the PVDF polymer. *Appl. Phys. A* **128**, 110 (2022). <https://doi.org/10.1007/s00339-021-05238-6>
  43. M.M. Arman, M.K. Ahmed, M.M. El-Masry, Cellulose Acetate polymer spectroscopic study comprised LaFeO<sub>3</sub> perovskite and graphene as a UV-to-visible light converter used in several applications. *J. Mol. Struct.* **1281**, 135153 (2023)
  44. L.J. Berchmans, R. Sindhu, S. Angappan, C.O. Augustin, Effect of antimony substitution on structural and electrical properties of LaFeO<sub>3</sub>. *J. Mater. Process. Technol.* **207**, 301 (2008)
  45. I. M. Aniz, M. Maisnam, H. S. Singh & C. Chaliha, Frequency dependence of dielectric and impedance properties of ZnO and TiO<sub>2</sub> added K<sub>0.5</sub>Na<sub>0.5</sub>NbO<sub>3</sub> ceramics. *Mater. Today: Proc.* (2023). <https://doi.org/10.1016/j.matpr.2023.02.299>
  46. X. Vendrell, J.E. García, X. Bril, D.A. Ochoa, L. Mestres, G. Dezanneau, Improving the functional properties of (K<sub>0.5</sub>Na<sub>0.5</sub>)NbO<sub>3</sub> piezoceramics by acceptor doping. *J. Eur. Ceramic Soc.* **35**(1), 125–130 (2015)
  47. E.E. Ateia, A.T. Mohamed, K. Elsayed, *J. Magn. Magn. Mater. Magn. Mater.* **452**, 169–178 (2018)
  48. M.A. Gilileo, *J. Phys. Chem. Solids Phys. Chem. Solids.* **13**, 33–39 (1960). [https://doi.org/10.1016/0022-3697\(60\)90124-4](https://doi.org/10.1016/0022-3697(60)90124-4)
  49. M. Chen, Y. Liu, W. Zhou, P. Wu, *Ceramics Int.* **49**, 7676–7682 (2023)
  50. E.C. Stoner, E.P. Wohlforth, *Philos. Trans. R. Soc. Lond. ALond. A* **240**(826), 599–642 (1948)
  51. E.E. Ateia, A.T. Mohamed, *J. Magn. Magn. Mater.* **426**, 217–224 (2017)
  52. A. Amirabadizadeh, T. Amirabadi, *WJCM* **3**, 131–135 (2013)

**Publisher's Note** Springer Nature remains neutral with regard to jurisdictional claims in published maps and institutional affiliations.